Disorder-induced topological transition in porous media flow networks

Norbert Stoop [a,b,1], Nicolas Waisbord [c,1], Vasily Kantsler [d], Vili Heinonen [a], Jeffrey S. Guasto [c,*],
Jörn Dunkel [a,*]

[a] *Department of Mathematics, Massachusetts Institute of Technology, 77 Massachusetts Avenue, Cambridge, MA 02139-4307, USA*
[b] *Institute of Building Materials, ETH Zürich, Stefano-Franscini-Platz 3, Zürich 8093, Switzerland*
[c] *Department of Mechanical Engineering, Tufts University, 200 College Avenue, Medford, MA 02155, USA*
[d] *Department of Physics, University of Warwick, Coventry CV4 7AL, UK*

ABSTRACT

We introduce spectral Morse–Smale analysis as a robust method to identify topological phase transitions in disordered continuous media. Combining microfluidic experiments with large-scale, pore-resolved simulations of porous media flow, we demonstrate that invariants of Morse–Smale graphs of flow speed provide a well-defined measure of the effects of spatial disorder on fluid transport. By systematically perturbing a microfluidic lattice, the fluid flow topology undergoes a phase transition from periodic to filamentous flow structure, which corresponds to a change in the spectral density of the Morse–Smale graphs and carries important implications for advective transport and front dispersion. Due to its generic formulation, spectral Morse–Smale analysis can be applied to detect and characterize topological transformations in a wide range of complex physical, chemical or biological fluid systems.

1. Introduction

Topology offers a robust framework to characterize complex physical phenomena by focusing on properties that remain invariant under continuous deformation. Topological approaches have proved powerful over a wide range of scales, from the detection of dark matter structures in the universe [1] and force network evolution in granular media [2–4] to the description of topological insulators [5], quantum computers [6] and DNA conformations [7,8]. The understanding of complex network structures, in particular, has benefited from such topological analyses [9,10]. These systems are effectively classified by their interaction topology and statistics [11–13], as in scale-free and small-world networks [9,14,15]. While topological analysis has been successfully employed in discrete settings, its applicability to pattern-formation and transport problems in continuous systems and complex fluids has remained relatively unexplored [16–18]. Here, we introduce the concept of spectral Morse–Smale (MS) analysis to identify topological phase transitions in disordered porous media flows, by merging ideas from spectral graph theory [19] with topological pattern recognition [20,21].

The MS complex [21] dissects a continuous scalar field $c(t, \mathbf{x})$, for example a concentration or flow-speed field, into domains of constant slope [20]. The resulting edge-graph encodes important topological information about the field configuration, and as we show here, the eigenvalue spectrum of a suitably weighted adjacency matrix can detect critical structural transitions in the network. We demonstrate the broad applicability of this analysis through both physical experiments and large-scale simulations, to show how flow structure evolves in the presence of increasing disorder within a quasi-2D porous medium. Traditional correlation measures struggle to disentangle geometric disorder in the porous matrix from inherent changes in the flow structure [22]. In contrast, the topological MS approach identifies a disorder-induced phase transition from localized to filamentous flow patterns through changes in the spectral density of the MS graphs. The application of this framework to polydisperse media with various porosities reveals that flow-filament formation relates directly to the anomalous transport properties of porous media flows [23]. These results illustrate the practical potential and broad applicability of spectral MS analysis for the characterization of emergent flow structures in complex fluids, and more generally of pattern formation in physical, chemical and biological continuum systems.

2. Topological Morse–Smale characterization of scalar functions

We use MS analysis to partition the domain of a given scalar function $\varphi : \Omega \rightarrow \mathbb{R}$. Below, φ is taken to be the flow speed field but in principle it could be any scalar observable. In theory, φ has to fulfill certain technical conditions (see Ref. [20]); these are however rather lax so that, in practice, the MS partitioning can be calculated for most φ. The first step in constructing the partitioning is to calculate all the extrema of φ; we denote the minima by $\mathbf{r}_i^{\min}$, the maxima by $\mathbf{r}_j^{\max}$, and the saddle points
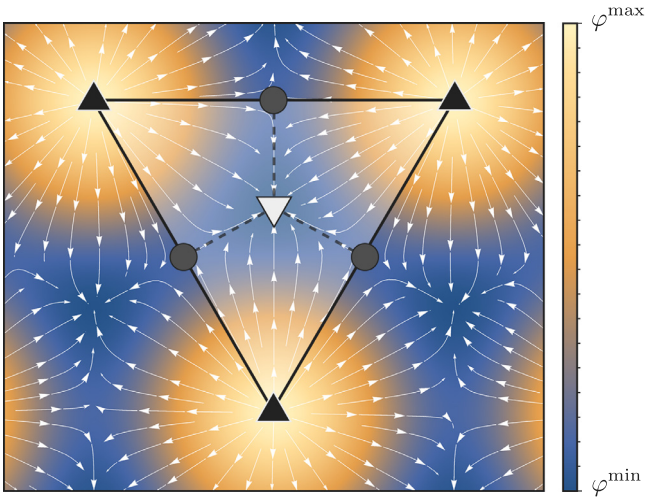

Fig. 1. Example of an ascending manifold around a single local minimum $\mathbf{r}_i^{\min}$ (indicated by the white triangle) of a function φ defined on a rectangular domain Ω. The white arrows show sample integral lines defined by Eq. (1) for various initial points $\mathbf{r}_0$. The black solid lines enclose the subdomain $\Omega_i^{\min}$ consisting of all the points that are taken by the gradient flow to the local minimum $\mathbf{r}_i^{\min}$ (white triangle) as $\tau \to \infty$. The boundary $\partial\Omega_i^{\min}$ is given by the graph (black solid lines) along which the integral lines go from maxima (black triangles) to saddle points (gray circles). The whole domain Ω of φ can be partitioned uniquely in this manner, yielding a graph of connected local maxima and saddle points. The dashed black lines further partition the ascending manifold into basic cells of the Morse–Smale (MS) complex.

by $\mathbf{r}_k^{\mathrm{sp}}$. Our goal is to partition the domain Ω of φ to subdomains $\Omega_i^{\min}$ that constitute the overall domain Ω. This can be achieved by introducing *integral lines* $\mathbf{r}(t; \mathbf{r}_0)$ of φ, defined as the paths satisfying the initial value problem

$$\partial_\tau \mathbf{r}(\tau) = -\nabla_\mathbf{r} \varphi(\mathbf{r}(\tau)), \quad \mathbf{r}(0) = \mathbf{r}_0, \tag{1}$$

where $\tau \geq 0$ parameterizes each path. Thus, according to Eq. (1), each $\mathbf{r}_0$ flows to a nearby local minimum $\mathbf{r}_i^{\min}$ by following the gradient of φ. We define $\Omega_i^{\min}$ as the set of points that are taken to the minimum $\mathbf{r}_i^{\min}$ as $\tau \to \infty$. Now, each boundary $\partial\Omega_i^{\min}$ consists of the gradient flows from the maxima surrounding $\mathbf{r}_i^{\min}$ to the saddle points on the boundary; see Fig. 1 for an example.

The maxima and the saddle points surrounding each of the minima define a graph containing the following information:

- Locations of the local maxima $\mathbf{r}_j^{\max}$ and the saddle points $\mathbf{r}_k^{\mathrm{sp}}$.
- Values of φ at $\mathbf{r}_j^{\max}$ and $\mathbf{r}_k^{\mathrm{sp}}$.
- Connectivity matrix between the nodes $\mathbf{r}_j^{\max}$ and $\mathbf{r}_k^{\mathrm{sp}}$.
- Distances between connected pairs of critical nodes $\mathbf{r}_j^{\max}$ and $\mathbf{r}_k^{\mathrm{sp}}$ along the integral lines.

This approach constitutes a discrete topological description of the function φ on Ω. The partitions $\Omega_i^{\min}$ are called the *ascending* manifolds. The *descending* manifolds $\Omega_j^{\max}$ can be defined similarly using the maxima and gradient ascent or by calculating the descending manifolds for $-\varphi$. The intersection of an ascending manifold $\Omega_i^{\min}$ and a neighboring descending manifold $\Omega_j^{\max}$ defines a cell of the MS complex. In the remainder, we only use the partitioning arising from the ascending manifolds $\Omega_i^{\min}$, corresponding to the large domain bounded by solid lines in Fig. 1, which consists of more than one MS-complex cell (smaller domains bounded by dashed lines in Fig. 1).

As an illustration, we calculated the MS complex for confined photoelastic disks under stress studied in Ref. [24] (Fig. 2). Photoelastic disks reveal the stress networks in granular packings, with brighter sections corresponding to higher stresses. Although the strength of the local stresses is a highly nonlinear function of brightness [24], the topological
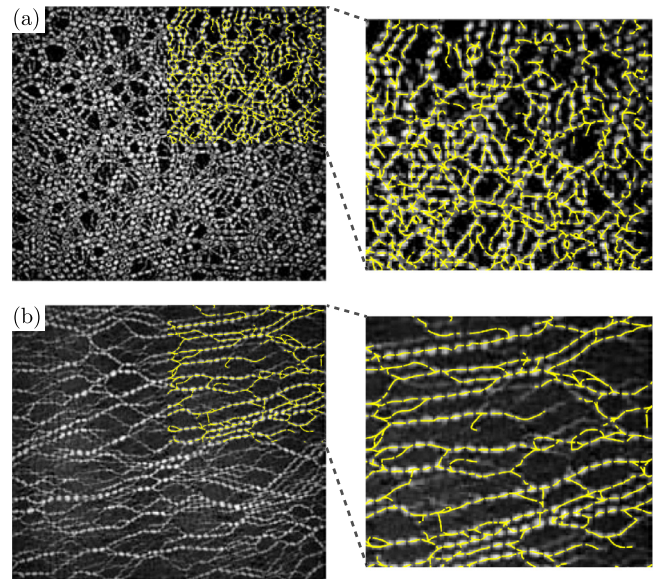

Fig. 2. Example of a MS complex showing the network encompassing the descending manifolds for stress chains in a granular medium of photoelastic disks with a diameter of 0.8 cm or 0.9 cm detailed in Ref. [24]: (a) shows biaxial compression while for (b) the compression is uniaxial. The bright areas correspond to high stress.

structure of the network can be readily extracted since the local maxima of the image brightness coincide with the maxima of the stress field. The system is compressed biaxially in Fig. 2a and uniaxially in Fig. 2b. The overlaid yellow lines indicate the reconstructed MS networks obtained with the DisPerSE [21] algorithm. These MS graphs encapsulate the relevant topological information [2–4] and structure of the underlying stress networks.

Below, we will apply this framework to identify and characterize the flow networks in disordered porous media, by studying the spectral properties of the associated MS graphs.

3. Experimental and numerical methods

To realize an experimental model system that exhibits a complex, continuous structure, we examine Stokes flow through a quasi-2D porous medium, which has applications to transport in biological tissues [25], filtering and industrial processes, and environmentally-relevant ground water flows [26]. Specifically, we are interested in analyzing how disorder in the porous medium affects the flow network topology.

3.1. Experiments

A series of microfluidic channels (height $h = 70$ μm, width $W = 2.5$ mm, length $L = 6.5$ mm) containing a 21×47 hexagonal array of cylindrical pillars (diameter 50 μm) were fabricated by soft-lithography [27] enabling precise control over the microstructural disorder of the quasi-2D porous medium (Fig. 3a; Appendix A). For each microchannel, pillar locations were perturbed on computer-generated photomasks from hexagonal lattice nodes (spacing $\ell = 120$ μm) with random displacements $\Delta \mathbf{x} = r \mathbf{s}$, where the vector $\mathbf{s}$ is uniformly sampled from the unit cell and $r \in \{0, 0.125, 0.25, 0.375, 0.5, 0.75, 1.0\}$ is the disorder amplitude ($r = 0$ corresponds to a perfect lattice). The porosity $\phi = V_{\mathrm{fluid}}/(V_{\mathrm{fluid}} + V_{\mathrm{pil}}) \approx 0.84$ was fixed, with V_{fluid} and V_{pil} denoting the total volumes of the fluid and pillars, respectively. A syringe pump supplied a 3 μl/min flow of DI water seeded with fluorescent tracer particles (0.5 μm diameter) through the porous microchannels. Individual tracers were tracked using video microscopy (Nikon Ti-e, $10\times$ 0.3 NA objective; Andor Zyla camera, 10 fps), and velocity fields were reconstructed using custom MATLAB codes (see also Appendix A).
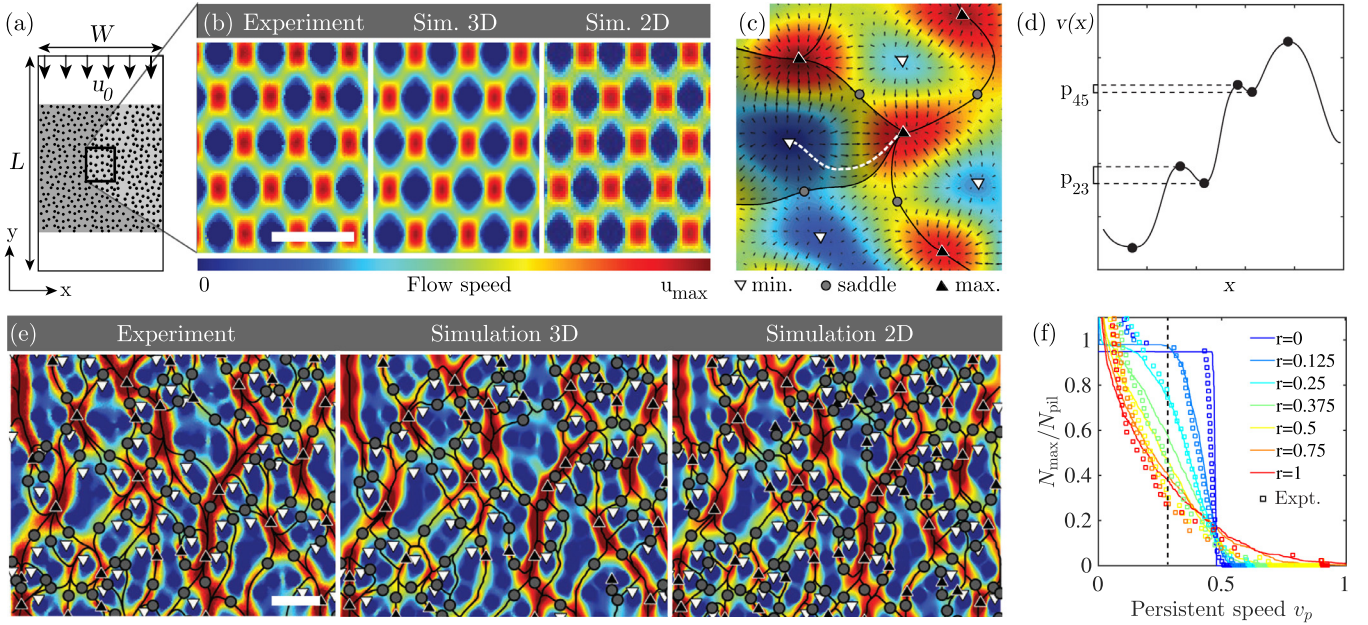
Fig. 3. Topological analysis of porous media flows. (a) Experimental and numerical porous microchannel geometry. Simulations use periodic boundary conditions in x-direction. (b) Experimental flow fields for a periodic lattice ($r = 0$) agree with 3D and 2D simulations. Only small subdomains are shown; see Appendix C for full-size simulations. Scale bar 150 μm. (c) MS-complex analysis on the flow-speed field identifies persistent flow structures by connecting maxima and saddle points through integral curves (illustration; black lines separate ascending manifolds). (d) The topological relevance of a connected pair (i, j) of critical points is measured by its (flow speed) persistence p_{ij} (illustration). (e) Randomized pillar positions ($r = 1$) favor the formation of high-speed flow field filaments. Ascending manifolds of the MS complex and extrema are shown for the persistence value $v_p \approx 0.3$, corresponding to the black dashed line in (f). Scale bar 150 μm. (f) The number of flow speed maxima N_{max} with persistence $\geq v_p$ in units of $u_{max} = 205$ μm/s, normalized by the total number of pillars N_{pil}, indicates a smooth transition in the MS complex from unperturbed ($r = 0$) to perturbed flow fields ($r = 1$). Deviations between experiments (□) and simulations (solid lines) indicate that measurement noise dominates below $v_p \approx 0.2$.

3.2. Simulations

The experiments validate large-scale simulations for pillar geometries identical to the microfluidic channels. We numerically solve the 3D Stokes equation [28] for the velocity field $\mathbf{u}(x, y, z)$ and the pressure $p(x, y, z)$,

$$\nabla \cdot \mathbf{u} = 0, \quad \mu \nabla^2 \mathbf{u} - \nabla p - \eta \rho(x, y)\mathbf{u} = 0 \quad (2)$$

where μ is the dynamic viscosity of water. No-slip boundary conditions on the pillar surfaces are enforced through the penalty-term $\eta \rho \mathbf{u}$, with $\rho(x, y) = 1$ inside a pillar and $\rho = 0$ otherwise. Large values of η enforce $\mathbf{u} = 0$ inside each pillar (in our simulations $\eta = 6.4 \cdot 10^5 \mu/h^2$). We adopt periodic boundary conditions along x and a fixed inlet velocity $\mathbf{u}(y = L) = (0, -u_0)$ (Fig. 3a).

Our experiments and 3D simulations focus on shallow channels, $h \ll W < L$, with no-slip boundaries at the top and bottom. In this case, numerical speed-up and larger simulation domains can be achieved by simulating an effective 2D model [29,30], obtained by assuming a Poiseuille flow profile along the z-direction,

$$\mathbf{u}(x, y, z) = \phi(z)\mathbf{v}(x, y)$$

with

$$\phi(z) = 6z(h - z)/h^2.$$

Inserting this ansatz into Eq. (2) and averaging along the z-direction yields the 2D Brinkman equations [29,30]

$$\bar{\nabla} \cdot \mathbf{v} = 0, \quad \mu(\bar{\nabla}^2 - k^2)\mathbf{v} - \bar{\nabla}\bar{p} + \eta \rho \mathbf{v} = 0, \quad (3)$$

with $k = \sqrt{12}/h$, $\bar{\nabla} = (\partial_x, \partial_y)$ and averaged pressure $\bar{p}(x, y)$. Although the 2D description is computationally advantageous, the Poiseuille approximation becomes inaccurate for densely packed pillar configurations. Eqs. (2) and (3) were solved using a stabilized finite element scheme

with local adaptive mesh refinement for improved accuracy [31], and compared to the microfluidic experiments (Fig. 3). For ordered lattices ($r = 0$), we find very good agreement between the periodic flow patterns observed in experiments, 3D and 2D simulations (Fig. 3b). Henceforth, all flow velocities are rescaled by $u_{max} = \max_{r=0} |\mathbf{u}| = 205$ μm/s for the ordered lattice. For strongly disordered systems ($r \to 1$), the velocity fields become irregular and high-speed filaments emerge (Fig. 3e) [22]. The continued agreement between experiments and simulations suggests that the Brinkman equation remains a useful approximation in the disordered regime (Fig. 3e).

3.3. Computing the Morse–Smale complex of the flow network

The MS complex of the 2D midplane flow-speed field $v(x, y) = |\mathbf{u}(x, y, h/2)|$ is computed using the DisPerSE [21] algorithm. After determining all critical points $\{(x_i, y_i)\}$ of v (triangles and circles in Fig. 3c), neighboring critical points are connected by integral lines defined by Eq. (1). Integral curves separating neighboring ascending manifolds connect the maxima along ridges of v (black curves in Fig. 3c). The *persistence* of a pair of critical points (i, j) is defined as the absolute difference of their field values (Fig. 3d)

$$p_{ij} = |v(x_i, y_i) - v(x_j, y_j)|. \quad (4)$$

Noise in the experimental data produces artificially low-persistence pairs, which can be removed in a hierarchical manner [21] by fixing a persistence threshold v_p. By reconnecting neighboring critical points with $p_{ij} > v_p$, one obtains a sparsified MS graph that preserves the topologically relevant features of v [32]. A detailed error analysis (Appendix B) shows that a meaningful topological analysis of the experimental flow fields should be restricted to structures with persistence $p_{ij} > v_{noise} \approx 0.2$ (Fig. 3f). However, the good agreement between experiments and simulations (Fig. 3e,f; Fig. C3) allows us to focus henceforth on the 'noise-free' 2D simulations.
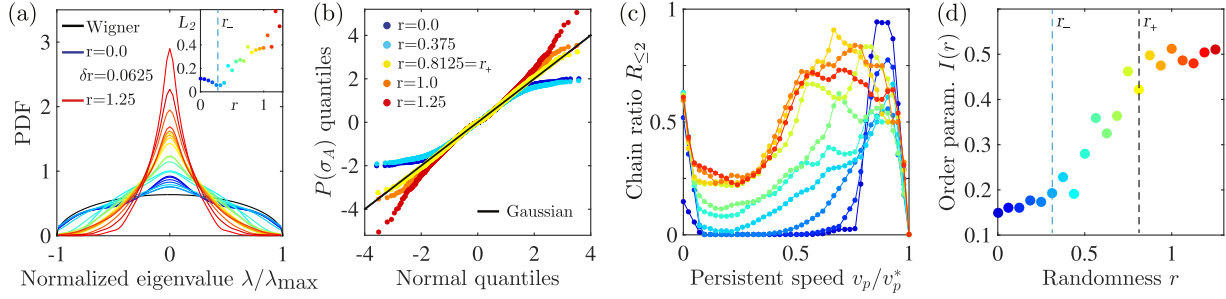
Fig. 4. Spectral properties of the Morse–Smale network ($v_p = 0.1$) signal a disorder-induced topological phase transition towards filamentous flow structures in 2D simulations. (a) The normalized spectral density first approaches and then departs from Wigner's semi-circle law (black line) with increasing disorder r. Inset: L_2-distance from the Wigner law, minimum occurs at $r_- \approx 0.31$. (b) The normalized quantiles of σ_A reveal a transition from short-tailed to long-tailed spectra at $r_+ \approx 0.81$ (yellow points); black line is a normal distribution. (c) The chain-link ratio $R_{\leq 2}$ of maxima with 2 or less outgoing edges signals persistent flow filaments at high disorder r. (d) The persistence-averaged order parameter $I(r) = \langle R_{\leq 2} \rangle$ calculated from (c), indicates the transition to filamentous flow structures with increasing r. Dashed vertical lines indicate the transition interval $[r_-, r_+]$, where r_- corresponds to the closest approach to the Wigner law in (a) and r_+ to the Gaussian spectral density in (b). (For interpretation of the references to colour in this figure legend, the reader is referred to the web version of this article.)

4. Results

4.1. Topological phase transition

The MS graph encapsulates the physically relevant information to identify topological phase transitions in generic pattern-forming systems. To probe the disorder-induced transition in our porous media model system, we perform a spectral analysis of the persistence-weighted adjacency matrix $A(v_p)$ of the flow speed MS graph for different disorder r. A is an $N \times N$-matrix, where $N = N_m + N_s$ is the number of maxima N_m and saddles N_s in the MS complex at persistence level v_p. The elements of A are defined as $A_{ij} = p_{ij}$ if the critical points i and j are connected, and $A_{ij} = 0$ otherwise. The MS graph represented by A is bipartite (maxima only connect to saddles, and *vice versa*), so that for each eigenvalue $\lambda_i > 0$ of A, its negative $-\lambda_i$ is also an eigenvalue and, hence, the mean

$$\frac{1}{N} \sum_i \lambda_i = 0.$$

The topological phase transition from periodic to filamentous flow patterns is indicated by a departure of the spectrum $\sigma_A = \{\lambda_i\}$ of A from Wigner's semicircle law [33]: For real symmetric $N \times N$-random matrices with independent, identically-distributed entries, the probability distribution function (PDF) of the normalized eigenvalues $\lambda/\lambda_{\max}$ approaches $\frac{1}{\pi}\sqrt{1 - \lambda/\lambda_{\max}}$ as $N \to \infty$. In contrast, the spectra of the MS adjacency matrix A from the porous media model first approach and then depart from this semicircle law as the disorder is increased from $r = 0$ to $r = 1.25$ (Fig. 4a). The departure from Wigner's law indicates that a supercritical disorder of $r > r_- \approx 0.31$ leads to correlations in the MS graph that correspond to the emergence of filamentous flow structures in the porous medium. A quantile analysis of the rescaled[2] spectral density of A shows an evolution from a short-tailed distribution for $r < r_+ \approx 0.81$ to a long-tailed distribution for $r > r_+$ (Fig. 4b). This qualitative change of the spectral density reflects the topological transition of the MS complex from a highly connected network with nearest-neighbor couplings to a sparser network with long filamentous paths.

4.2. Chain links & filaments

The development of filamentous flow structures during the topological phase transition is also evident in the 'chain-link' ratio $R_{\leq 2}$ defined as the number of maxima with two or fewer outgoing edges in the MS

complex divided by the total number of maxima. If $R_{\leq 2}$ is large, then the network consists of many successively linked maxima and saddles, indicating that fluid transport is dominated by fluid filaments (Fig. 3e). Our numerical results for $R_{\leq 2}$ confirm that filamentous structures become more persistent with increasing disorder r (Fig. 4c). The transition can be described in terms of the order parameter $I(r) = \langle R_{\leq 2} \rangle$, where the average is taken over persistence-values $0 \leq v_p \leq v_p^*$, with v_p^* denoting the maximum persistence above which the graph cannot be further simplified. That is, $I(r)$ corresponds to the average height of the curves in Fig. 4(c). The order parameter I sharply increases in the interval $[r_-, r_+]$, demonstrating (*i*) that the onset of filament formation coincides with the departure from Wigner's law and (*ii*) that the transition is "complete" when the spectral density of the MS adjacency matrix has become long-tailed (Fig. 4b,d).

4.3. Polydisperse media

Pore geometry dictates anomalous transport through the formation of filamentous flow structures, which we elucidate through topological MS analysis. Simulated flow structures are compared for different pillar geometries:

- (MR) mono-disperse random with $r = 1.0$;
- (PO) polydisperse ordered hexagonal lattice with normally distributed pillar diameters (mean $\langle d \rangle = 50\ \mu m$; variance $\sigma = \ell/2$) permitting for a small obstacle-overlap probability;
- (PR) polydisperse-random with same pillar size distribution as PO but randomized positions with $r = 1.0$;
- (PR*) polydisperse-random with $r = 1.0$ but large pillar size variation ($\langle d \rangle = 50\ \mu m$; $\sigma = 2\ell$).

Simulations were performed for porosities $\phi_1 = 0.84$ (MR, PO, PR) and $\phi_2 = 0.65$ (MR, PO, PR, PR*); see Appendix C for details. The structure of the simulated fluid velocity fields suggests that filament formation is more pronounced in low porosity media compared to higher porosities (Figs. 5a,b and D1), which is confirmed quantitatively by measuring the chain length $R_{\leq 2}$ as a function of persistence (Figs. 5c and D2 a). Accordingly, the order parameter values for low porosity $0.6 \leq I_{\phi_2} \leq 0.66$ are significantly larger than for high porosity $0.47 \leq I_{\phi_1} \leq 0.52$ (Fig. 5c). The MS graph structures become more complex at lower porosity, which is evident from the persistence-averaged number of maxima in chains $\langle N_{\leq 2}^{\max} \rangle$ (Figs. 5c and D2b).

Consistent with traditional correlation-based approaches [34–36], the filamentous character of porous media flows directly affects the transport properties of these systems. By constructing the streamlines in each medium, we calculated the front dispersion

$$\sigma_Y^2 = \langle [Y(t/t_{\text{pil}}) - \langle Y(t/t_{\text{pil}}) \rangle]^2 \rangle / \langle d \rangle^2,$$

---

[2] All spectra were rescaled to match the ± 3 quantiles of a standard normal distribution, so that a Gaussian normal distribution corresponds to a line of slope 1 in Fig. 4(b).
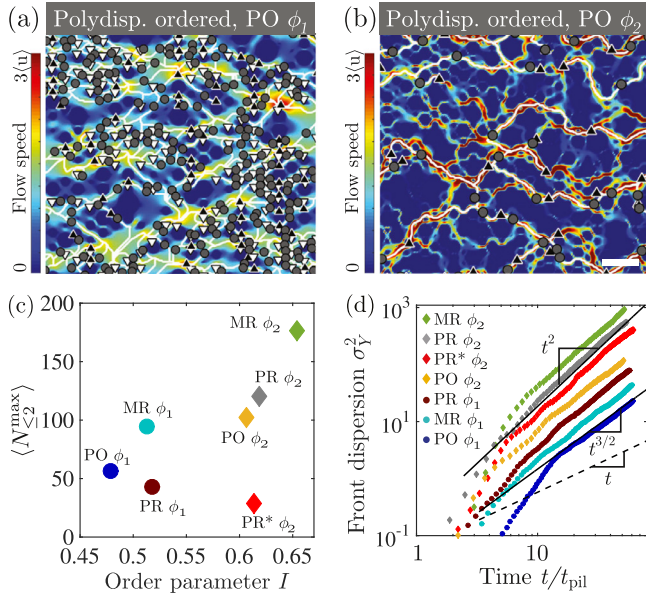
Fig. 5. Simulated flow through a polydisperse, ordered lattice at porosity $\phi_1 = 0.84$ (a) and porosity $\phi_2 = 0.65$ (b). Scale bar 300 µm. MS complex persistence is $v_p/v_p^* = 1/3$. Colorbars are capped at $3\langle u \rangle$ to visualize flow channels. (c) The filament order parameter $I = \langle R_{\leq 2} \rangle$ confirms that low porosity geometries ($\diamondsuit$) provide more filamentous flows independent of the type of spatial disorder. (d) Front dispersion is affected by filamentous flow structures, with almost ballistic transport for low porosities, and smaller exponents $\sim t^{3/2}$ for equally sized media at higher porosities. Diffusive transport ($\sim t$) shown for reference.
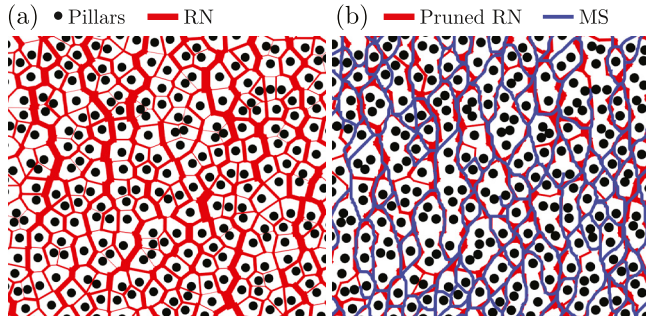

Fig. 6. Morse–Smale (MS) complex and 'pruned' resistor network (RN) with equivalent number of links share similar graph structure. (a) Complete RN approximation to a monodisperse porous medium. Line thickness is proportional to conductance. (b) Pruned RN with MS complex overlaid. (For interpretation of the references to color in this figure legend, the reader is referred to the web version of this article.)

where $Y(t)$ is the y-position of a fluid particle at time t, $t_{\rm pil}$ is the average time to advect a distance $\langle d \rangle$, and $\langle \cdot \rangle$ denotes the average over 1000 randomly chosen streamlines. After initial transients, when spatial disorder becomes relevant, the less filamentous flows at high porosities ϕ_1 exhibit smaller transport exponents, $\sigma_Y^2 \sim (t/t_{\rm pil})^{3/2}$ consistent with random walk models in stratified fluids [37], whereas front-diffusion in low porosity media is asymptotically *ballistic* even at a large times (Fig. 5d). Thus, flow filament distributions dictate the transport properties of porous media [38–42].

The MS complex is representative of the dominant fluid flow pathways through the porous medium, explaining the strong correlation with the physical transport properties. We consider a simplified resistor network model of the porous medium (Fig. 6a). The boundaries of the Voronoi cells around the pillars define a network approximation of the pore-links, and the nodes correspond to the pores $i = 1, \ldots, N_p$. Trans-

port between nodes i and j is represented by the flux matrix element Q_{ij} and the pore pressure at i by P_i. Incompressible flow through the network is governed by Kirchhoff's rule

$$\sum_{j \in \mathcal{N}(i)} Q_{ij} = 0,$$

where $\mathcal{N}(i)$ denotes the neighbors of i, and Ohm's law

$$Q_{ij} = C_{ij}(P_i - P_j).$$

Adopting a Poiseuille approximation and assuming a rectangular pore-link geometry (length $l_{ij} \sim d$, width w_{ij}, height h), the conductances are [43]

$$C_{ij} = \frac{\min(h, w_{ij})^2}{4\mu d} \left[\frac{1}{3} - \frac{64\epsilon_{ij}}{\pi^5} \tanh\left(\frac{2\pi}{\epsilon_{ij}}\right) \right] \quad (5)$$

where $\epsilon_{ij} = \min(h/w_{ij}, w_{ij}/h)$ and solutions are obtained through matrix inversion. To compare directly the fluid pathways between the simplified network model and the MS complex for a given persistence v_p, we iteratively 'prune' the network by first deleting the link carrying the lowest flux and subsequently recomputing the flow through the reduced network. Fig. 6b shows a pruned resistor network (red) with 28% of the links removed to match approximately the number of links in the corresponding MS network, which is overlaid (blue). The agreement between the two networks illustrates that the MS complex captures the primary transport routes through the medium.

5. Discussion and conclusions

We have introduced spectral Morse–Smale (MS) analysis to identify topological transitions in porous media flows. The underlying methodology can be straightforwardly applied to time-dependent and multi-species flows in 2D and 3D, and could offer new insights into the effects of flow network topology on Taylor–Aris dispersion [44–46]. While we focused here on the MS transport graph of the flow speed field, topological networks of other observables, including pressure, concentration, and more, can be constructed in an analogous manner. Their associated weighted-graph spectra will typically carry useful information about the distribution of dissipative or diffusive fluxes. To illustrate this briefly for an idealized scenario, let us consider a 3D porous media flow $\mathbf{u}$ with viscosity μ and slip boundary conditions, so that gradients transverse to flow channel directions can be neglected. In this case, the spectrum of the persistence-weighted adjacency matrix can be linked to dissipation as follows: the dissipated power $\mathcal{P}_{ij}$ of the flow between vertices i and j of the MS graph connecting maxima and saddles can be expressed as

$$\mathcal{P}_{ij} = \mu \int_{\Omega_{ij}} d\mathbf{r} \, \|\nabla \mathbf{u}\|^2,$$

where Ω_{ij} is a fluid cell enclosing the MS path (ij) between vertices i and j, and $\|\nabla \mathbf{u}\|$ is the Frobenius norm of the flow gradient tensor. Let $|\Omega_{ij}|$ be the volume of the cell Ω_{ij} and l_{ij} the distance between i and j. Assuming that the velocity field in Ω_{ij} is aligned with (ij) and neglecting transverse gradients, we may approximate

$$\mathcal{P}_{ij} \approx \mu |\Omega_{ij}| \frac{|\mathbf{u}_i - \mathbf{u}_j|^2}{l_{ij}^2} \approx \mu |\Omega_{ij}| \frac{|u_i - u_j|^2}{l_{ij}^2},$$

where $u_i = |\mathbf{u}_i|$ denotes the flow speed at the location of vertex i of the MS graph. Note that $|\mathbf{u}_i - \mathbf{u}_j| \approx |u_i - u_j|$ because an (ij)-aligned velocity field cannot reverse its direction between a speed maximum i and adjacent saddles j. The geometric factor $w_{ij} = |\Omega_{ij}|/l_{ij}^2$ defines an effective transverse length scale of the flow channel enclosing the MS path (ij). Given the actual diameters w_i and w_j of the flow channels at the MS vertex positions i and j, we can approximate w_{ij} by the geometric mean $w_{ij} \approx \min(w_i, w_j) \approx \sqrt{w_i w_j}$. Abbreviating $\sqrt{w_i} = \psi_i$, the total dissipation power can be written as the sum over all branches (ij) as

$$\sum_{(ij)} \mathcal{P}_{ij} \approx \mu \sum_{(ij)} \psi_i |u_i - u_j|^2 \psi_j =: \mathcal{P}.$$

Noting that

$$u_p \le |u_i - u_j| \le u_{\max}$$

where u_p is the persistence speed (level) and $u_{\max}$ the flow speed maximum, we can bound $\mathcal{P}$ by

$$u_p \sum_{(ij)} \psi_i |u_i - u_j| \psi_j \le \frac{\mathcal{P}}{\mu} \le u_{\max} \sum_{(ij)} \psi_i |u_i - u_j| \psi_j.$$

In terms of the persistence-weighted adjacency matrix A_{ij} as defined above, this inequality can be rewritten as

$$\frac{u_p}{2} \sum_{i,j} \psi_i A_{ij} \psi_j \le \frac{\mathcal{P}}{\mu} \le \frac{u_{\max}}{2} \sum_{i,j} \psi_i A_{ij} \psi_j.$$

The matrix A_{ij} is real and symmetric, implying that its eigenvalues λ_n are real and that the eigenvectors $\psi^{(n)}$ can be chosen orthonormal. Expanding $\psi_i = \sum_n c_n \psi_i^{(n)}$, with the system-dependent coefficients c_n describing the channel (pore) widths, the upper and lower dissipation bounds become

$$\frac{1}{2} u_p \sum_n c_n^2 \lambda_n \le \frac{\mathcal{P}}{\mu} \le \frac{1}{2} u_{\max} \sum_n c_n^2 \lambda_n.$$

Thus, in this setting, a spectrum $\{\lambda_n\}$ peaked around zero corresponds to a system in which the majority of flow channels exhibit small dissipation. Analogous physical interpretations may be achievable in other applications depending on the observable chosen to construct the Morse–Smale complex.

In conclusion, the underlying mathematical framework renders the techniques introduced here broadly applicable to study topological transitions in a wide range of equilibrium and non-equilibrium systems, including non-Newtonian and unsteady fluid flows. The above discussion demonstrates that the Morse–Smale complex robustly captures the underlying flow structure in ordered and disordered porous media, providing a new methodology to understand transport in these systems. More generally, the spectral analysis of Morse–Smale complex networks has the potential to yield new insights into stress propagation in active gels [47] and granular media [2–4,48,49], to identify morphological changes in biological tissues [50], and to characterize pattern-formation transitions in reacting chemical systems [51] and complex fluids [52].

Acknowledgments

Appendix A. Experiments

The setup of our microfluidics experiments is shown in Fig. A1. Polydimethylsiloxane (PDMS) channels were fabricated using soft lithography [27], where each channel has a height $h = 70$ μm, width $W = 2.5$ mm and length $L = 6.5$ mm, and contains an array of 21×47 cylindrical pillars (diameter 50 μm) in their central region (Fig. 3a). The pillars form a randomized hexagonal lattice in the (x, y)-plane (lattice spacing $\ell = 120$ Âμm, porosity $\phi = 0.84$). Pillar positions are determined by adding random displacements $\Delta \mathbf{x} = r \mathbf{s}$ to the nodes of a perfect hexagonal lattice. The random vectors $\mathbf{s}$ are uniformly distributed in the unit cell. The parameter $r \in \{0, 0.125, \ldots, 1\}$ determines the degree of disorder: $r = 0$ corresponds to a perfectly ordered lattice, whereas for $r = 1$ pillar centers can be placed everywhere within a unit cell around the lattice nodes. Photolithography is used to create PDMS molds using high resolution photomasks from the computer-generated pillar geometry. PDMS microchannels are initially filled with alcohol to avoid bubble formation. A syringe pump (Harvard Apparatus, PHD Ultra) drives a suspension of fluorescent tracer particles (0.5 μm diameter; Invitrogen),

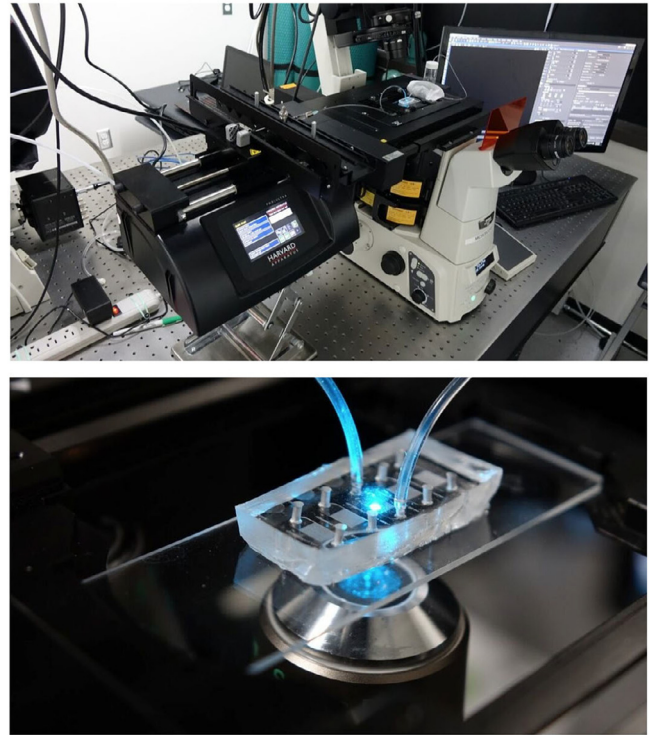**Fig. A1.** Experimental setup (top) and microfluidic device (bottom). For scale, the microfluidic device is fabricated on a standard 25 mm × 75 mm microscope slide.
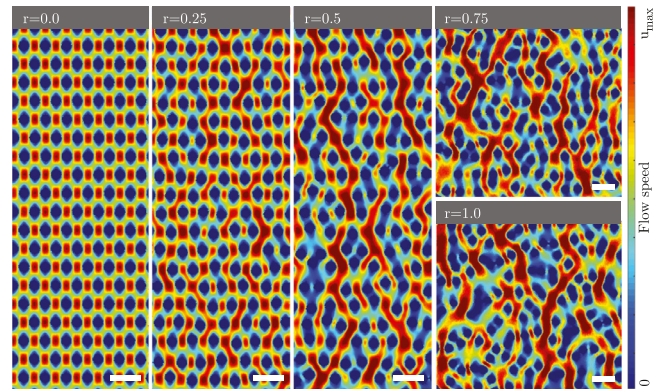

Fig. A2. Representative examples of flow speed fields measured in our experiments for different values of the disorder parameter r. Color bar: $u_{\max} = 205$ μm/s. Flow direction: from top to bottom. Scale bars 150 μm.

which are suspended in DI water (0.16 μl of 2% v/v tracer particle solution per ml of water) with 0.1% bovine serum albumen to prevent particle adhesion to the microchannel surfaces. Particle suspensions are driven at a flow rate of 3 μl/min and the tracer motion is recorded using an epifluorescence microscope (Nikon Ti-e; 10× 0.3 NA objective) at 10 fps (Andor Zyla camera). The focal depth of the imaging system was ≈ 7.5 μm and the field of view was 1664 μm × 1404 μm. Individual tracers were tracked and the velocity fields reconstructed using custom MATLAB algorithms (Fig. A2).

Appendix B. Estimating noise in experimental data

Spectral MS analysis can be used to determine noise levels in the experimental data. To demonstrate this, we compare basic properties of the MS complexes for experimental and numerical speeds v, varying

$r \in [0, 1]$. In the ordered limit case $r = 0$, N_{pil} pillars cause $N_{max} = N_{pil}$ maxima in v (Fig. 3f). This suggests that we may study the normalized density of maxima $\rho_{max} = N_{max}/N_{pil}$ as a domain-size-independent order parameter. Plotting ρ_{max} as function of the persistence cutoff v_p shows good agreement between experiments and 2D simulations for $v_p \gtrsim 0.2$ (Fig. 3f). We therefore conclude that the measurement noise in the experiments falls below the persistence threshold $v_{noise} \approx 0.2$, implying that a meaningful MS analysis of the experimental data should be restricted to topological structures of persistence $p_{ij} > v_{noise}$.

Appendix C. Experiments *vs.* simulations

Spectral MS analysis detects topological differences between experimental and numerical data, when other standard measures become insensitive. To illustrate this, we consider the relative local error $\varepsilon(x, y) = (v_{sim} - v_{exp})/v_{exp}$ between flow speeds measured in experiments and simulations. For both 3D simulations (Fig. C1) and 2D simulations (Fig. C2), we find that ε is dominated by deviations near pillar boundaries (Fig. C3a,b), masking systematic differences between the

Fig. C3. Topological error estimation using Morse–Smale analysis. (a,b) The local relative error $\varepsilon = (v_{exp} - v_{sim})/v_{exp}$ between experimentally and numerically obtained flow speeds is dominated by deviations near pillar boundaries for both 3D and 2D simulations. (c) The distribution of ε provides little insight into the quality of either simulation type. (d,e) Small but persistent deviations in the flow field (in units of $u_{max} = 205$ μm) are made apparent by comparing the Morse–Smale graph of experiments and 2D simulations. (f) The spectral error ε_σ defined in the text indicates that 3D simulations reproduce experimentally observed flow structures consistently better than 2D simulations. Scale bar: 150 μm.
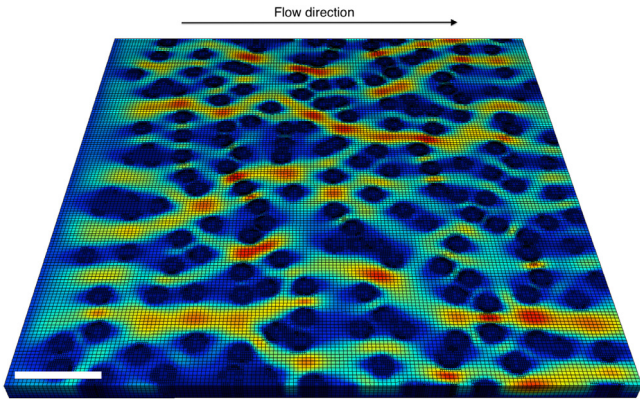

Fig. C1. Result of a 3D simulation with disorder parameter $r = 1$ using a local adaptive mesh (black grid lines). Scale bar 150 μm.
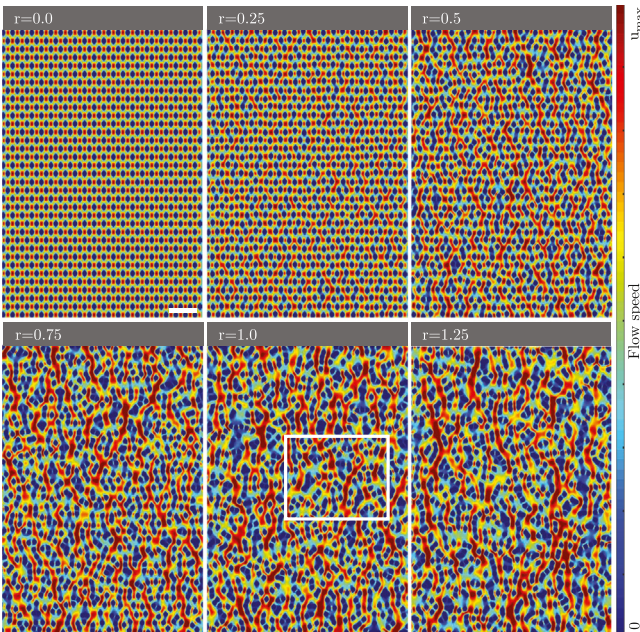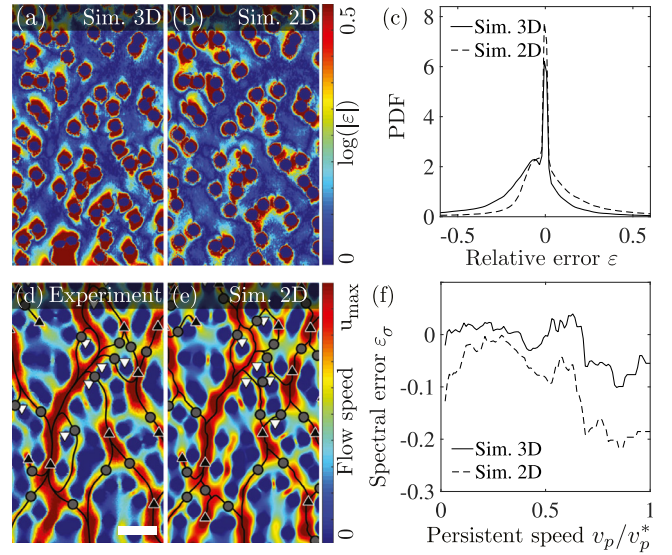

Fig. C2. Representative examples of flow fields obtained in our 2D simulations of the Brinkman model for different values of the disorder parameter r. The white rectangle indicates the subdomain shown in Fig. 1e of the Main Text. Color bar: $u_{max} = 205$ μm/s. Flow direction: from top to bottom. Scale bar 300 μm.

2D and the 3D model, as evident from the nearly identical probability density functions (PDFs) in Fig. C3c. To obtain a more sensitive topological similarity measure, we compare the MS complex for flow-speed data from experiments with 3D and 2D simulations at various persistence levels $v_p \in [0, v_p^*]$, where $v_p^* \approx 1.21$ is the maximum persistent speed beyond which the descending manifold complex cannot be simplified further. Visual inspection reveals that, in contrast to the local error measure ε, the descending manifolds reflect local deviations between experiments and 2D simulations already at intermediate persistence levels $v_p \sim 0.5$ (Fig. C3d,e). These differences are encoded in the eigenvalue spectrum $\sigma_A = \{\lambda_i\}$ of the persistence-weighted adjacency matrix A of the underlying MS graph structures. A is an $N \times N$-matrix, where $N = N_m + N_s$ is the total number of maxima N_m and saddles N_s in the MS complex at persistence level v_p. We define $A_{ij} = p_{ij}$ if the critical points i and j are connected, and $A_{ij} = 0$ otherwise. The graph represented by A is bipartite (maxima only connect to saddles, and *vice versa*), so that for each eigenvalue $\lambda_i > 0$ of A, $-\lambda_i$ is also an eigenvalue and, hence, the mean $\langle \sigma_A \rangle = 0$. We therefore consider the variance $\langle \sigma_A^2 \rangle$ to define the relative spectral error between experiment and simulation as $\varepsilon_\sigma = 1 - \langle \sigma_{A_{sim}}^2 \rangle / \langle \sigma_{A_{exp}}^2 \rangle$. Plotting ε_σ for 2D and 3D simulations demonstrates that the 3D model better reproduces the experimentally measured flow topology over the entire persistence range $[0, v_p^*]$. However, despite significant deviations at high persistence levels, the 2D simulations still provide a reasonable approximation to the 3D flow topology at intermediate values of $v_p/v_p^* \leq 0.7$. In the remainder, we will focus on the 2D model which makes it possible to simulate macroscale media efficiently.

Appendix D. Porosity affects filament formation

To study the effect of porosity and disorder on filament formation in porous media flows, we compare the $r = 1.0$ medium at porosity $\phi_1 = 0.84$ (MD, ϕ_1) to an equivalent medium with $r = 1.0$, pillar diameter $d = 50$ μm, but lower average pillar spacing, resulting in lower porosity
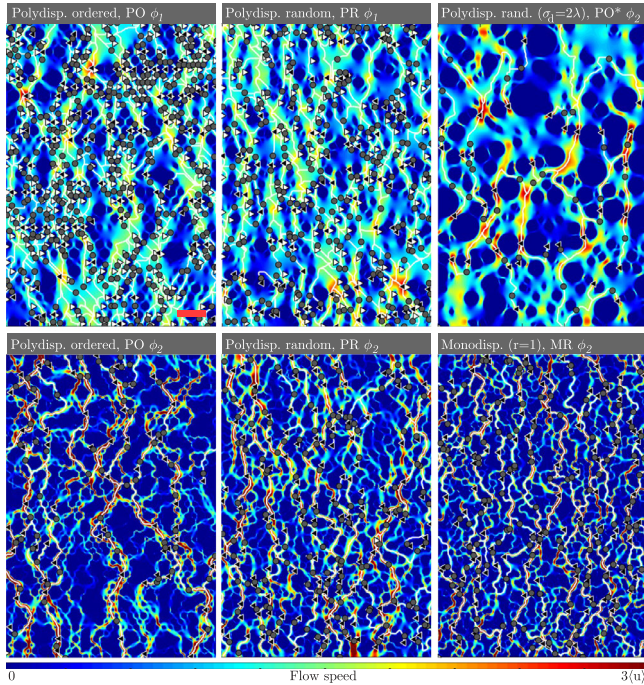
Fig. D1. Simulated flow through porous media at porosities $\phi_1 = 0.84$ and $\phi_2 = 0.65$ for polydisperse ordered (PO), polydisperse random (PR, PR*) and monodisperse media with $r = 1.0$ (MR). Lower porosities (ϕ_2, higher pillar density) favor the formation of filaments and dead zones for all randomizations considered. For improved visualization of channels, colorbars are capped at $3\langle u \rangle$, where $\langle u \rangle$ is the average fluid speed in the fluid domain. Scale bar 300 µm.

Fig. D2. (a) Flow through porous media at low porosities (ϕ_2) leads to larger filament chain ratios $R_{\leq 2}$, with small dependence on the type of random media (MR: monodisperse random, PO: polydisperse ordered, PR: polydisperse random, PR* polydisperse random with larger pillar size fluctuations). (b) The graph complexity, measured by the number of maxima forming filament chains, $N_{\leq 2}^{\max}$ for a given persistence v_p, generally increases with lower porosity, as indicated by the averages $\langle N_{\leq 2}^{\max} \rangle$ over $0 \leq v_p \leq v_p^*$ (horizontal lines).

$\phi_2 = 0.65$ (MR, ϕ_2). We further consider media of the same porosity but with different types of disorder.

Polydisperse-ordered media (PO) Starting from an ordered hexagonal lattice with pillar diameter $d = 50$ µm and porosities ϕ_1 or ϕ_2, the pillar diameters are drawn from a Gaussian distribution with $\langle d \rangle = 50$ µm and variance $\sigma = \ell/2$. To correct for slight changes in the porosity after randomization of the pillar diameters, all pillars are uniformly rescaled in diameter to match either porosity ϕ_1 or ϕ_2. This rescaling is typically associated with changing the pillar diameter by less than 3% and hence, to good approximation, does not change the average pillar diameter.

Polydisperse-random media (PR) Random-polydisperse media with the same pillar diameter distributions as in the PO media are generated by randomly placing the pillars of a PO medium of porosity ϕ_1 or ϕ_2 in sequential order. A position in the channel is chosen from a uniform random distribution and a pillar is placed if there is no overlap with previously placed pillars. To guarantee packing of all pillars even at low porosities, pillars are placed in descending order of their diameters.

Polydisperse random media with large pillar fluctuations (PR)* To study the effects of larger fluctuations in the pillar diameters, we additionally consider pillars with $\langle d \rangle = 50$ µm and variance $\sigma = 2\ell$, placed in sequential order as in PR media. After each pillar placement, the current porosity is calculated and placement of new pillars stops once the target porosity is reached. Due to the large pillar size fluctuations, PR* media at high porosities ϕ_1 contain only a few pillars. Considerably larger system sizes would thus be needed to study their transport behavior. We therefore only consider PR* at low porosity $\phi_2 = 0.65$.

The numerically computed flow fields suggest lower porosities increase channel formation in porous media flows for all considered random porous media (Fig. D1). This feature is confirmed quantitatively by the chain-link ratio $R_{\leq 2}$ and its average $I = \langle R_{\leq 2} \rangle$ (Fig. D2), showing generally higher values of I for low porosity media, irrespective of the type of disorder. To study how the type of disorder affects the MS complex within all media of same porosity, we consider the total number
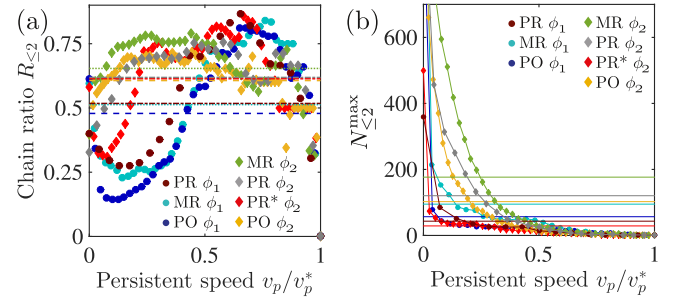
of maxima being part of chain-like filaments, $N_{\leq 2}^{\max}$, i.e. maxima with only two or less connected neighbors, as function of the persistence v_p (Fig. D2b). Its average over all persistences, $\langle N_{\leq 2}^{\max} \rangle$ (horizontal lines in Fig. D2b) indicates that for either porosity ϕ_1 and ϕ_2, monodisperse random media (MR) result in the most complex filament structures, followed by polydisperse random (PR) and polydisperse ordered media (PO), which have similar complexities for given porosity. PR* has lowest graph complexity of all media, despite its low porosity. When comparing flow fields of the entire simulation domain (Fig. D1), the PO* flow field appears to be considerably less isotropic than those of the other media, suggesting that the MS graph complexity could provide an alternative measure of the homogeneity of porous media flows at different length scales.

References

[1] T. Sousbie, C. Pichon, H. Kawahara, The persistent cosmic web and its filamentary structure - II. illustrations, Mon. Not. R. Astron. Soc. 414 (1) (2011) 384–403.

[2] M. Kramár, A. Goullet, L. Kondic, K. Mischaikow, Evolution of force networks in dense particulate media, Phys. Rev. E 90 (2014) 052203.

[3] M. Kramár, A. Goullet, L. Kondic, K. Mischaikow, Quantifying force networks in particulate systems, Phys. D 283 (2014) 37–55.

[4] T. Takahashi, A.H. Clark, T. Majmudar, L. Kondic, Granular response to impact: topology of the force networks, Phys. Rev. E 97 (2018) 012906.

[5] C.L. Kane, E.J. Mele, Z2 topological order and the quantum spin hall effect, Phys. Rev. Lett. 95 (14) (2005) 146802.

[6] S.D. Sarma, M. Freedman, C. Nayak, Topologically protected qubits from a possible non-abelian fractional quantum hall state, Phys. Rev. Lett. 94 (16) (2005) 166802.

[7] S. Wasserman, N. Cozzarelli, Biochemical topology: applications to DNA recombination and replication, Science 232 (4753) (1986) 951–960.

[8] P. Brown, N. Cozzarelli, A sign inversion mechanism for enzymatic supercoiling of DNA, Science 206 (4422) (1979) 1081–1083.

[9] R. Albert, A.L. Barabási, Statistical mechanics of complex networks, Rev. Mod. Phys. 74 (1) (2002) 47–97.

[10] S. Boccaletti, V. Latora, Y. Moreno, M. Chavez, D. Hwang, Complex networks: structure and dynamics, Phys. Rep. 424 (4–5) (2006) 175–308.

[11] D. Watts, S. Strogatz, Collective dynamics of 'small-world' networks, Nature 393 (6684) (1998) 440–442.

[12] H. Jeong, S. Mason, A.L. Barabási, Z. Oltvai, Lethality and centrality in protein networks, Nature 411 (6833) (2001) 41–42.

[13] C. Schneider, A. Moreira, J. Andrade, S. Havlin, H. Herrmann, Mitigation of malicious attacks on networks, Proc. Natl. Acad. Sci. USA 108 (10) (2011) 3838–3841.

[14] A.L. Barabási, R. Albert, Emergence of scaling in random networks, Science 286 (5439) (1999) 11.

[15] R. Cohen, S. Havlin, Scale-free networks are ultrasmall, Phys. Rev. Lett. 90 (5) (2003) 058701.

[16] F. Corson, E.D. Siggia, Geometry, epistasis, and developmental patterning, Proc. Natl. Acad. Sci. USA 9 (15) (2012) 5568–5575.

[17] D.R. Lester, G. Metcalfe, M.G. Trefry, Is chaotic advection inherent to porous media flow? Phys. Rev. Lett. 111 (2013) 174101.

[18] H. Kusumaatmaja, Surveying the free energy landscapes of continuum models: application to soft matter systems, J. Chem. Phys. 142 (2015) 124112.

[19] R.A. Brunaldi, The mutually beneficial relationship of graphs and matrices, in: CBMS Regional Conference Series in Mathematics, American Mathematical Society, Providence, R.I., 115, 2011.

[20] A. Zomorodian, Topology for computing, vol. 53, 2005.

[21] T. Sousbie, The persistent cosmic web and its filamentary structure - i. theory and implementation, Mon. Not. R. Astron. Soc. 414 (1) (2011) 350–383.

[22] S.S. Datta, H. Chiang, T.S. Ramakrishnan, D.A. Weitz, Spatial fluctuations of fluid velocities in flow through a three-dimensional porous medium, Phys. Rev. Lett. 111 (2013) 064501.

[23] D.R. Lester, G. Metcalfe, M.G. Trefry, Anomalous transport and chaotic advection in homogeneous porous media, Phys. Rev. E 90 (2014) 063012.

[24] T.S. Majmudar, R.P. Behringer, Contact force measurements and stress-induced anisotropy in granular materials, Nature 435 (7045) (2005) 1079–1082.

[25] A.R. Khaled, K. Vafai, The role of porous media in modeling flow and heat transfer in biological tissues, Int. J. Heat Mass Transf. 46 (26) (2003) 4989–5003.

[26] B. Berkowitz, Characterizing flow and transport in fractured geological media: a review, Adv. Water Resour. 25 (8–12) (2002) 861–884.

[27] Y. Xia, G.M. Whitesides, Soft lithography, Ann. Rev. Mater. Sci. 28 (1) (1998) 153–184.

[28] L. Landau, E. Lifshitz, Fluid Mechanics, 6, Pergamon Press, 1987.

[29] H.C. Brinkman, A calculation of the viscous force exerted by a flowing fluid on a dense swarm of particles, Appl. Sci. Res. 1 (1) (1949) 27–34.

[30] M. Nagel, F. Gallaire, Boundary elements method for microfluidic two-phase flows in shallow channels, Comput. Fluids 107 (2015) 272–284.

[31] W. Bangerth, R. Hartmann, G. Kanschat, Deal.II—a general-purpose object-oriented finite element library, ACM Trans. Math. Softw. 33 (4) (2007). 24–es

[32] D. Laney, P.T. Bremer, A. Mascarenhas, P. Miller, V. Pascucci, Understanding the structure of the turbulent mixing layer in hydrodynamic instabilities, IEEE Trans. Vis. Comput. Graphics 12 (5) (2006) 1053–1060.

[33] E. Wigner, Random matrices in physics, SIAM Rev. 9 (1) (1967) 1–23.

[34] P. de Anna, T.L. Borgne, M. Dentz, A. Tartakovsky, D. Bolster, P. Davy, Flow intermittency, dispersion, and correlated continuous time random walks in porous media, Phys. Rev. Lett. 110 (2013) 184502.

[35] P. Kang, P. de Anna, J. Nunes, B. Bijeljic, M. Blunt, R. Juanes, Pore-scale intermittent velocity structure underpinning anomalous transport through 3-d porous media, Geophys. Res. Lett. 41 (17) (2014) 6184–6190.

[36] T.L. Borgne, D. Bolster, M. Dentz, P. de Anna, A. Tartakovsky, Effective pore-scale dispersion upscaling with a correlated continuous time random walk approach, Water Resour. Res. 47 (12) (2011) w12538.

[37] D. Sornette, Critical phenomena in natural sciences: chaos, fractals, selforganization and disorder: concepts and tools, Springer Science & Business Media, 2006.

[38] J. Jiménez-Martínez, P. de Anna, H. Tabuteau, R. Turuban, T.L. Borgne, Y. Méheust, Pore-scale mechanisms for the enhancement of mixing in unsaturated porous media and implications for chemical reactions, Geophys. Res. Lett. 42 (13) (2015) 5316–5324.

[39] J.R. de Dreuzy, J. Carrera, M. Dentz, T.L. Borgne, Time evolution of mixing in heterogeneous porous media, Water Resour. Res. 48 (6) (2012). W06511

[40] T.L. Borgne, M. Dentz, E. Villermaux, Stretching, coalescence, and mixing in porous media, Phys. Rev. Lett. 110 (2013) 204501.

[41] P. Kang, T.L. Borgne, M. Dentz, O. Bour, R. Juanes, Impact of velocity correlation and distribution on transport in fractured media: field evidence and theoretical model, Water Resour. Res. 51 (2) (2015) 940–959.

[42] P. de Anna, M. Dentz, A. Tartakovsky, T.L. Borgne, The filamentary structure of mixing fronts and its control on reaction kinetics in porous media flows, Geophys. Res. Lett. 41 (13) (2014) 4586–4593.

[43] J. Berthier, P. Silberzan, Microfluidics for Biotechnology, Artech House, Boston, 2010.

[44] R. Aris, On the dispersion of a solute in a fluid flowing through a tube, Proc. Royal Soc. A 235 (1956) 67–77.

[45] I. Frankel, H. Brenner, On the foundations of generalized taylor dispersion theory, J. Fluid Mech. 204 (1989) 97–119.

[46] M. Aminian, F. Bernardi, R. Camassa, D.M. Harris, R.M. McLaughlin, How boundaries shape chemical delivery in microfluidics, Science 354 (6317) (2016) 1252–1256.

[47] F. Backouche, L. Haviv, D. Groswasser, A. Bernheim-Groswasser, Active gels: dynamics of patterning and self-organization, Phys. Biol. 3 (4) (2006) 264–273.

[48] D. Howell, R. Behringer, C. Veje, Stress fluctuations in a 2d granular couette experiment: a continuous transition, Phys. Rev. Lett. 82 (1999) 5241–5244.

[49] O. Ramos, E. Altshuler, K.J. Måløy, Avalanche prediction in a self-organized pile of beads, Phys. Rev. Lett. 102 (2009) 078701.

[50] G. Usuku, J. Gross, Morphologic studies of connective tissue resorption in the tail fin of metamorphosing bullfrog tadpole, Dev. Biol. 11 (3) (1965) 352–370.

[51] C.R. Nugent, W.M. Quarles, T.H. Solomon, Experimental studies of pattern formation in a reaction-advection-diffusion system, Phys. Rev. Lett. 93 (2004) 218301.

[52] M.C. Marchetti, J.F. Joanny, S. Ramaswamy, T.B. Liverpool, J. Prost, M. Rao, R.A. Simha, Hydrodynamics of soft active matter, Rev. Mod. Phys. 85 (2013) 1143–1189.